604889

COPY 2 OF 3
HARD COPY $. 2.00
MICROFICHE $. 0.50

37p

Measurement of Fluid Properties for Magnetoplasmadynamic Power Generators

Fifth Quarterly Technical Summary Report

(1 May — 31 July 1964)

Contract No. Nonr-4104(00) and Amendment 1

Order No.: ARPA 420 Project Code No. 3980

Engineering Department Report No. 3965

Allison Division

General Motors Corporation

Indianapolis, Indiana

DDC
RECEIVED
TISIA E

MISSING PAGE NUMBERS ARE BLANK AND WERE NOT FILMED

Measurement of Fluid Properties for Magnetoplasmadynamic Power Generators

Fifth Quarterly Technical Summary Report

(1 May — 31 July 1964)

Contract No. Nonr-4104(00) and Amendment 1

Order No.: ARPA 420 Project Code No. 3980

Engineering Department Report No. 3965

17 August 1964

Written By:

R. T. Schneider,
Program Manager

Approved:

F. G. Myers
Research Director

FOREWORD

This technical summary report was prepared by the Research Department of the Allison Division of General Motors Corporation. The work reported was accomplished under Contract Nonr-4104(00) and Amendment No. 1 thereto.

The program was sponsored by the Advanced Research and Project Agency through the Power Branch of the Office of Naval Research under the direction of ARPA and Mr. J. A. Satkowski of ONR.

Allison personnel who contributed material for this report are:

H. E. Wilhelm
R. O. Whitaker
R. L. Koch

TABLE OF CONTENTS

Section	Title	Page
I	Introduction	1
II	Summary of Work Accomplished	3
	Construction of Closed Loop Device	3
	Test Runs	3
	Design of a Larger Test Section	4
III	Experimental Arrangement	5
	Instrumentation	5
	Electrode Types	7
IV	Typical Data	11
V	Discussion of Results	21
	Voltage-Current Curves	21
	Saturation Effect	29
	Conclusions	33

LIST OF ILLUSTRATIONS

Figure	Title	Page
1	Recording instrumentation circuit diagram	6
2	Pin type electrode	7
3	Continuous (plate) electrode	7
4	Segmented electrodes	7
5	Original recording—run 9	13
6	Original recording—run 4	15
7	Original recording—run 8A	17
8	Voltage-current curve for generator with continuous electrodes	21
9	Power output curve for data of Figure 8	22
10	Voltage-current curve for generator with segmented electrodes	23
11	Power output curve for data of Figure 10	24
12	Faraday generator equivalent circuit	25
13	Segmented electrode generator equivalent circuit	26
14	Saturation effect for continuous electrode generator	30
15	Saturation effect for segmented electrode generator	30

I. INTRODUCTION

This report reviews the accomplishments achieved on Contract ONR Nonr-4104(00) during the past three months. It has been found that at low field strengths the generator voltage is proportional to the magnetic field strength. With increasing field strength the voltage deviates from this proportionality and finally saturates. A possible explanation of this phenomena is presented herein. The definition of one of the generator operational problems will allow a logical attack on the imposed limitations.

The closed loop research facility has undergone several modifications to improve the operational and control characteristics. The design of the generator for Phase II of the contract has been initiated.

II. SUMMARY OF WORK ACCOMPLISHED

CONSTRUCTION OF CLOSED LOOP DEVICE

During the report period the cesium injection system was improved further. In addition to the existing sight glass, a constant displacement pump was added to measure and better control the cesium mass flow. The stroke of this pump is variable, so that the desired mass flow can be preset. Pump strokes will be recorded together with the output data of the generator. Therefore, two independent methods of measuring cesium mass flow now exist.

It has been found necessary to further improve the system which separates the helium and cesium. It now appears that the cesium remains suspended in the helium in the form of a dust even after it has been cooled to nearly room temperature. Therefore, a large settling tank was added to the existing vortex separators, where the gas velocity has been reduced sufficiently to allow the cesium dust to settle. The tank can be heated between runs so that the cesium can be melted and drained to a collection tank.

TEST RUNS

A large number of test runs with cesium-seeded helium were made. The following electrode types were tested: protruding pins, continuous electrodes (plates), and segmented electrodes.

The main results of the runs to date can be summarized as follows.

- A saturation effect of the power output was observed. Above a magnetic field strength of 10,000 gauss the power output increases only slightly and finally saturates. This effect has been observed for both continuous and segmented electrodes. The investigation and elimination of this effect by additional experiments is one of the most important objectives in the coming program.
- All observed voltage-current curves are straight lines. This is true for directly plotted curves as well as for curves compiled from different runs. The straight lines indicate that no appreciable electron heating (magnetically induced ionization) has been observed.
- Neglecting possible leak resistance and boundry layer effects, the observed conductivity is 1 mho/m for a gas temperature of 1700°K, which is very near the equilibrium conductivity.

DESIGN OF A LARGER TEST SECTION

The outcome of the theoretical investigations indicate that to observe nonequilibrium effects, the duct length must be at least 10 cm. During the reporting period the design of a new MHD test section (including a heater) has been initiated. The 30,000-gauss magnet was also slightly modified to allow a channel length of 15 to 20 cm. Calibration runs will be made in the very near future to find a reasonable compromise between channel length and field strength.

The design goal for the electrode spacing (channel height) is 5 cm.

III. EXPERIMENTAL ARRANGEMENT

INSTRUMENTATION

Recent experience has shown the importance of recording generator output data together with certain characteristic operation parameters of the device as functions of time. It is also important to synchronize all observed data as closely as possible. An Offner 8-channel strip chart recorder was used for those runs made during the reporting period. Figure 1 shows the circuit diagram of the 8-channel recorder and related instrumentation.

Channel 1 recorded helium flow rate, measured by the pressure difference across an orifice flowmeter. A Statham type DC-00-350 differential pressure unit transducer incorporating a strain gage bridge was used at the flowmeter. The bridge drive was obtained from the input coupler of the recorder.

Channel 2 recorded the field excitation of the MHD electromagnet by measuring the voltage drop across a resistor in series with the field coils. This voltage drop was directly proportional to the field current. Due to nonlinearities in the magnetic structure, field current is not directly proportional to magnetic field and must be determined by a calibration curve. Incorporation of the function generator of an analog computer into the instrumentation channel is now being considered. Setting up the calibration curve on the function generator would cause the recorder trace to indicate magnetic field directly.

Channel 3 recorded the voltage across the main heater.

Channel 4 recorded heater current, by recording the voltage drop across a resistor in series with the heater. Heater temperature (and thus resistance) is purely a function of current; a calibration curve of power input versus heater current could be prepared. Heater temperature is also a function of helium flow, however. Consequently, both heater current and heater voltage were recorded so that heater input power could be determined.

Channel 5 recorded the output voltage of the first pair of electrode segments. Power output may be calculated once this voltage and the load resistance are known.

Channels 6, 7, and 8 recorded the output voltages of the remaining electrode segments.

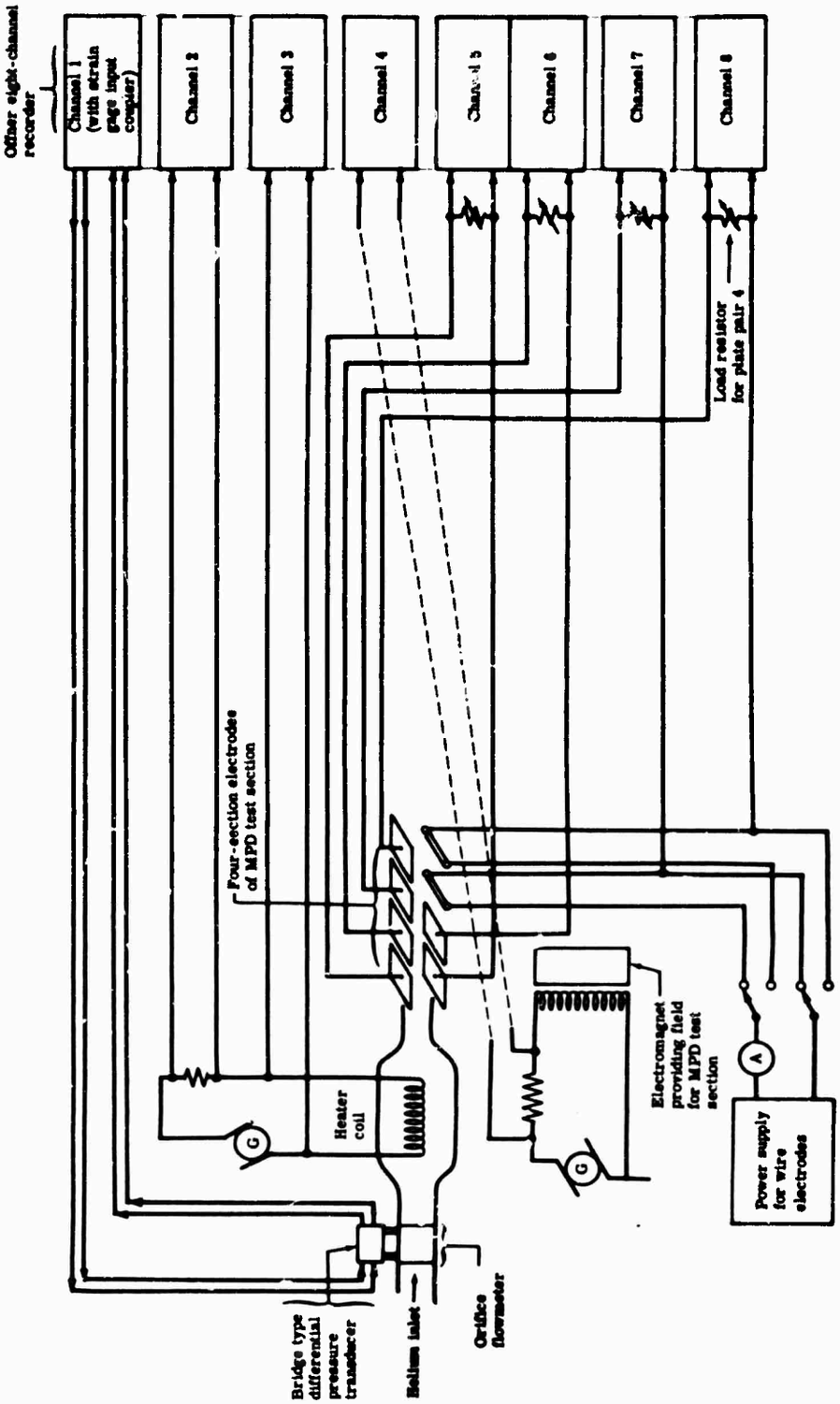

Figure 1. Recording instrumentation circuit diagram.

BLANK PAGE

ELECTRODE TYPES

The different types of electrodes used for the runs to date are shown in Figures 2, 3, and 4.

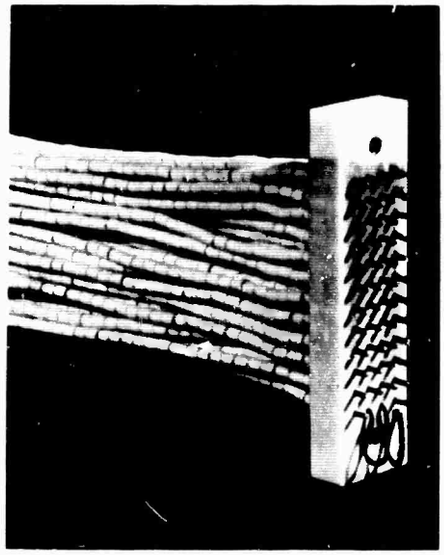

Figure 2. Pin type electrode.

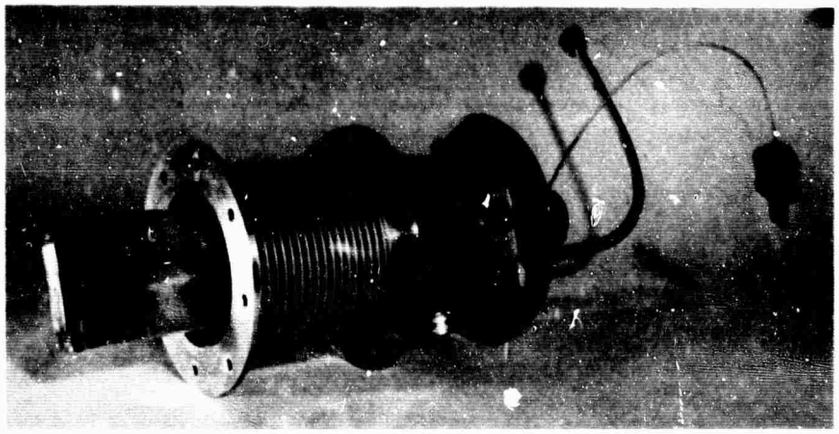

Figure 3. Continuous (plate) electrode.

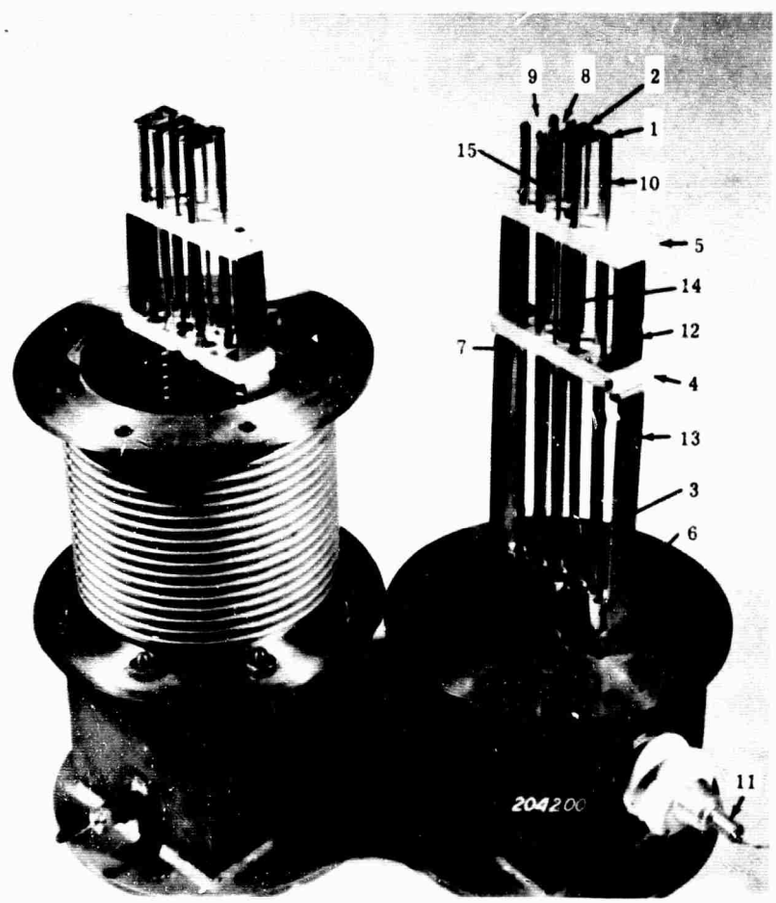

Figure 4. Segmented electrodes.

The performance of the electrodes in Figures 2 and 3 was discussed in earlier reports. The experience obtained in runs with the other two electrodes was applied during the design of the electrode shown in Figure 4. The main concern in the new design was to avoid leakage resistance between the electrodes and ground. Such leakage resistance probably occurs because at high temperatures the ceramic becomes a conductor and/or because tungsten evaporated from the heater is deposited on the ceramic parts, forming a conducting surface layer. Therefore, the electrode was so designed that ceramic parts are as far as possible from the hot gas stream.

Details of the electrode structure can be seen at the right of Figure 4. The segments (1), (2) were tungsten strips approximately 0.3 mm thick, 14 mm long, and 6 mm wide, heliarc welded at the ends to 3 mm dia (approximate) tungsten rods.

Tungsten rods were silver soldered to copper leads as indicated (3).

Copper leads were held rigidly in position laterally by ceramic sleeves (6) which wedged into the opening in the base of the electrode structure.

Tungsten rods were positioned longitudinally by nickel strips spot welded to the rods as indicated (7). Copper leads were bent and biased upward so that these nickel strips bore against the underside of the block (4).

Tungsten wires (8), (9) were welded to the third and fourth rod pairs. These wires could be heated electrically to provide thermionic emission.

A tungsten igniter rod (10) extended approximately 4 mm above the level of the electrode segments. It was anticipated that this electrode would be used to provide an initiating spark at the head of the test section. The rod connected to the high voltage terminal (11).

The electrode assembly at the left of Figure 4 is identical to the one at right except for the electrodes on the third and fourth rod pairs. Since this electrode assembly was to be the anode, it was not necessary for the segments to be thermionic emitters.

Considerable effort was expended before a satisfactory structure was finally completed. Heliarc welding of the tungsten strips to the tungsten rods proved particularly difficult.

The spacer (12) was made of tantalum. The bracket (13) was made of stainless steel.

The holes (14) in the alumina blocks were employed in another application of the blocks. For the current tests the holes were plugged with tantalum slugs. Rods (15), positioned next to these holes, were of reduced diameter to retain as much wall strength as possible.

BLANK PAGE

IV. TYPICAL DATA

This section discusses typical raw data recordings. An evaluation of all technical data and a discussion of the results are given in Section V.

On the three recordings shown (Figures 5, 6, and 7), the traces are in the following order, from top to bottom:

1. The pressure difference on the orifice flowmeter, Δp—related to the helium mass flow (gm/sec) by a calibration curve

2. Current through the magnet coils—connected with the magnetic field strength (gauss) through a calibration curve

3. Heater voltage—direct measurement of voltage drop on the heater

4. Heater current—measurement of current through the heater by voltage measurement across a shunt

5 through 8. Electrodes

On the electrode traces (5 through 8) the zero line is in the center of the recording space; on all other traces the zero line is at the bottom of the recording space.

Figure 5 shows a run (9) with a medium seeding fraction. The magnetic field was kept constant. The load resistor of electrode 1 was varied, while the load resistors of the other electrodes were kept constant (500 ohms). It is interesting to note the relationships of the four electrodes.

Sudden increases in conductivity occur for some unknown reason. These are shown as humps on all four traces. (See time = 6 and 10 sec.) The amplitude of the humps decrease slightly from electrode to electrode, which is reasonable. With the relatively slow recording equipment used, the humps appear to occur simultaneously. If faster recording methods were used, however, the possible time shift of the humps could well be used to measure gas velocity. In this case, of course, such conductivity fluctuations would be created artificially. Such a run is scheduled to be conducted during the next report period. At the time t = 22 sec another such

hump occurs, seemingly from such a sudden increase in conductivity. This hump, however, does not seem to occur at electrode 1. This can be explained by the fact that at this point in time, electrode 1 is loaded by a low load resistor. At the time t = 34 and 36 sec (and at several other times) electrode 1 was short circuited for a short time. This disturbed the neighboring electrodes. Yet the amplitude of this disturbance decreases much faster than the type of disturbance mentioned previously. This phenomenon is discussed in the next section.

Figure 6 shows a run (4) with a very large seed fraction. The most striking observation in this run are the cyclic nature of the power output and helium mass flow. The two parameters are definitely correlated, since the sharp dip in the helium mass flow occurs simultaneously with the small dip in the power output (about halfway between the minimum and maximum values of the power output vibration). Judging from this and other recordings taken, there also seems to be a correlation with the magnetic field, although this fact has not yet been established clearly. If a relationship exists between the vibration and the magnetic field, then it is certainly a very complicated relationship. It appears that the frequency of the oscillations may depend on the magnetic field strength. Also, the position of the small dip in the power output oscillation relative to the maximum and minimum seems to be dependent upon the magnetic field.

One question arises—that of whether or not the observed oscillation in the helium mass flow is real (whether or not the mass flow really drops to approximately half its value for a short time and then recovers). Possibly, due to explosive vaporization of the cesium, a pressure wave is created which travels back into the pipes and causes the Δp gage on the orifice flowmeter to read erroneous values. Considering the details of the piping, however, this is most unlikely. It seems much more reasonable to consider that the drop in helium mass flow is real. In hesitating to attribute this drop in mass flow to the braking action on the $\vec{j} \times B$ forces, it must be assumed that (due to the excess high cesium mass flow applied in this type of run) not all cesium is vaporized in the core section of the heater. Some cesium would thus enter the nozzle in the form of droplets, where it would be mixed with the hot helium. This in turn would cause the cesium droplets to vaporize explosively in the nozzle, raising the pressure in the nozzle for a short time and temporarily halting the helium mass flow. This, of course, would not depend on the applied magnetic field.

It is therefore very important to determine whether the observed fluctuations in helium mass flow depend on the magnetic field. Considerably more data must be gathered before this question can be resolved.

BLANK PAGE

A

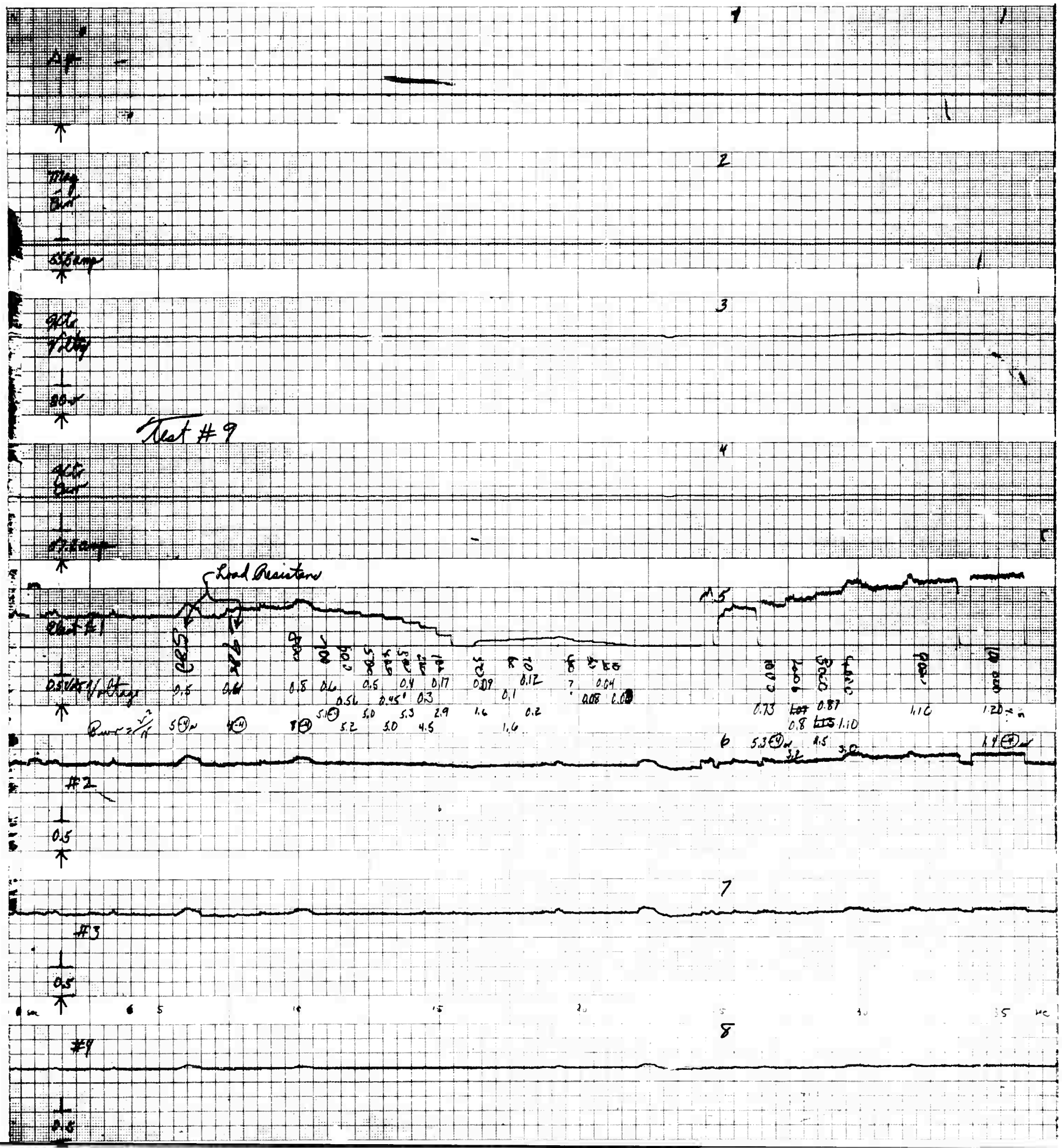

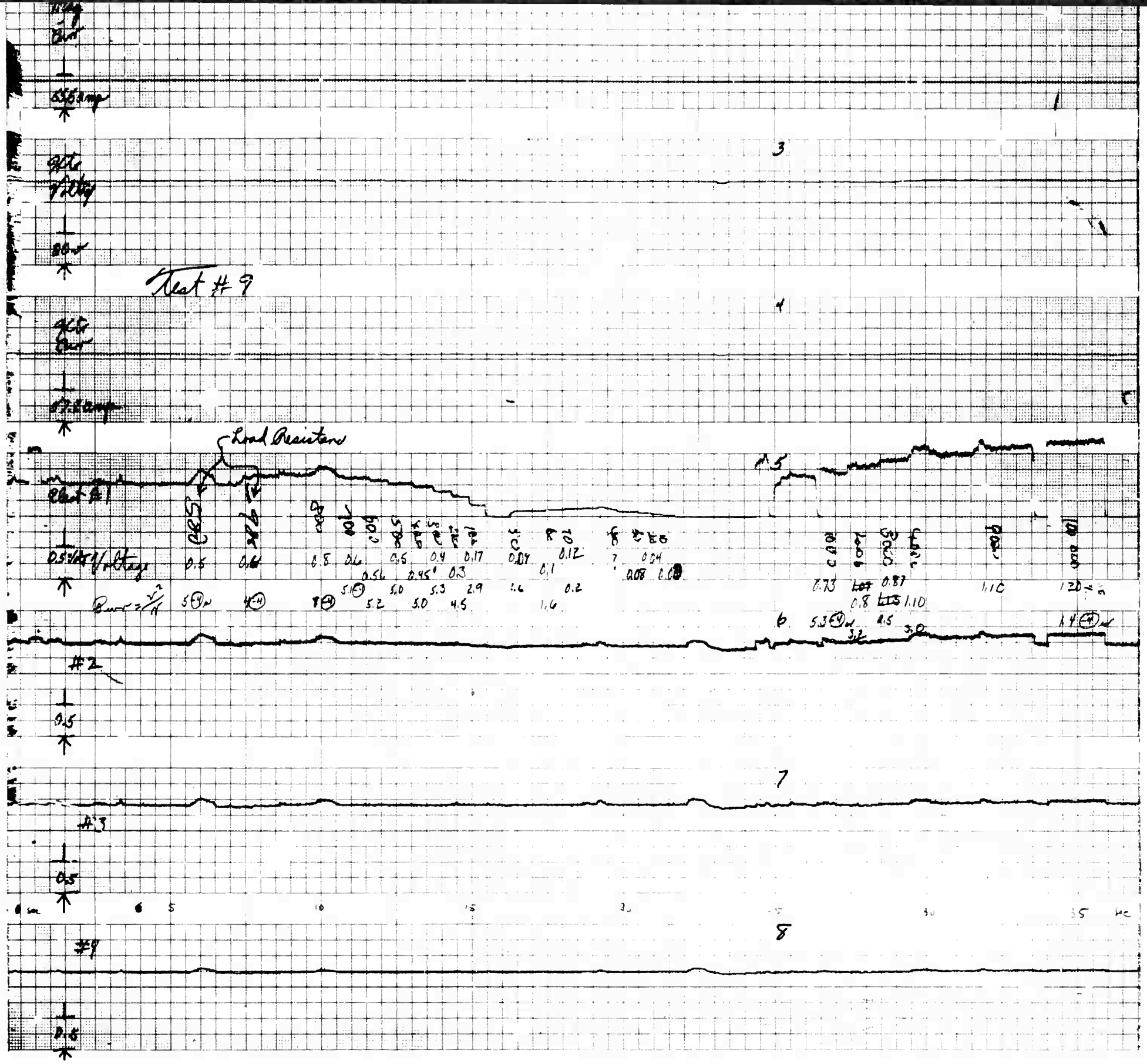

Figure 5. Original recording—run 9.

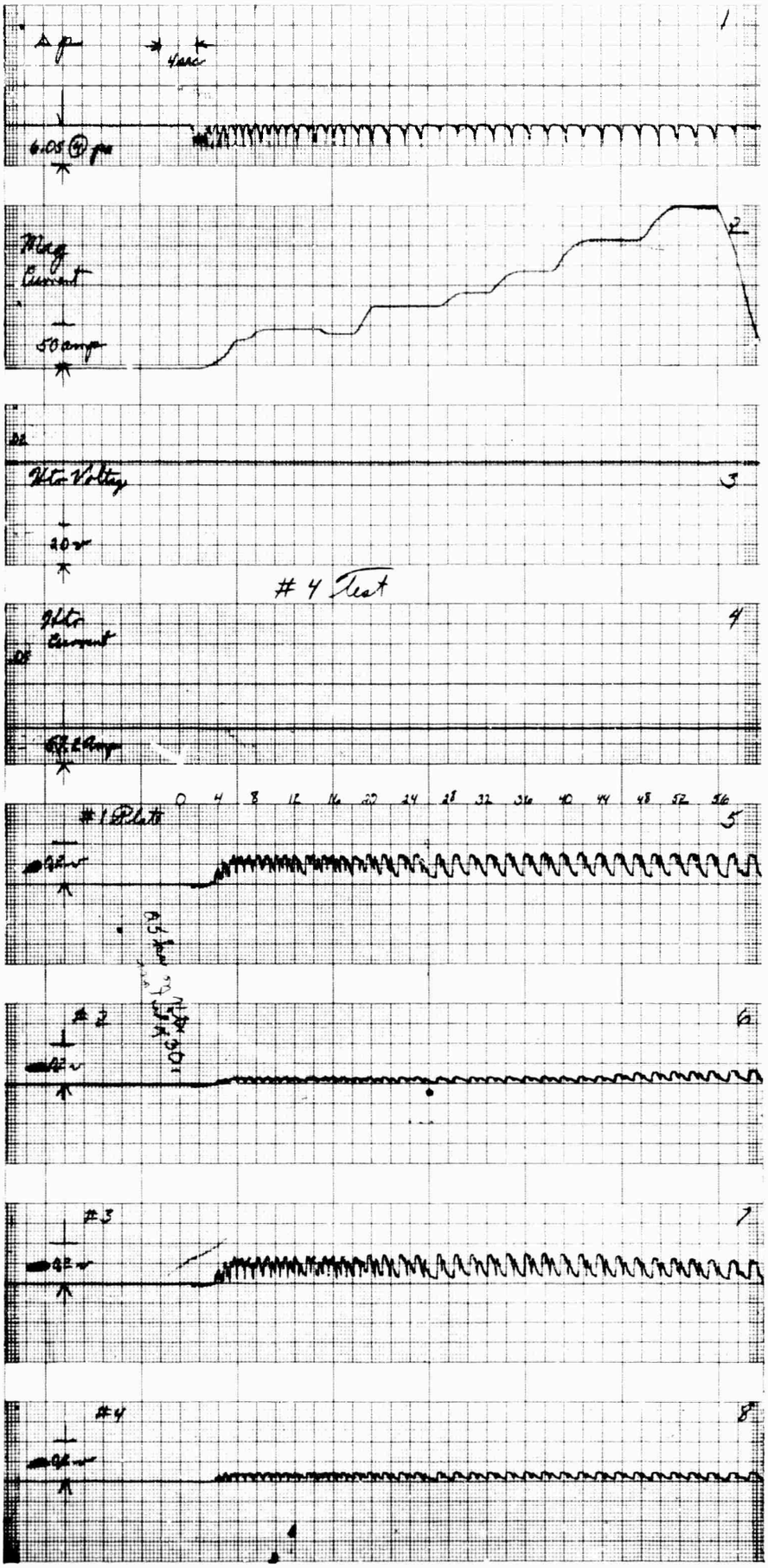

Figure 6. Original recording—run 4.

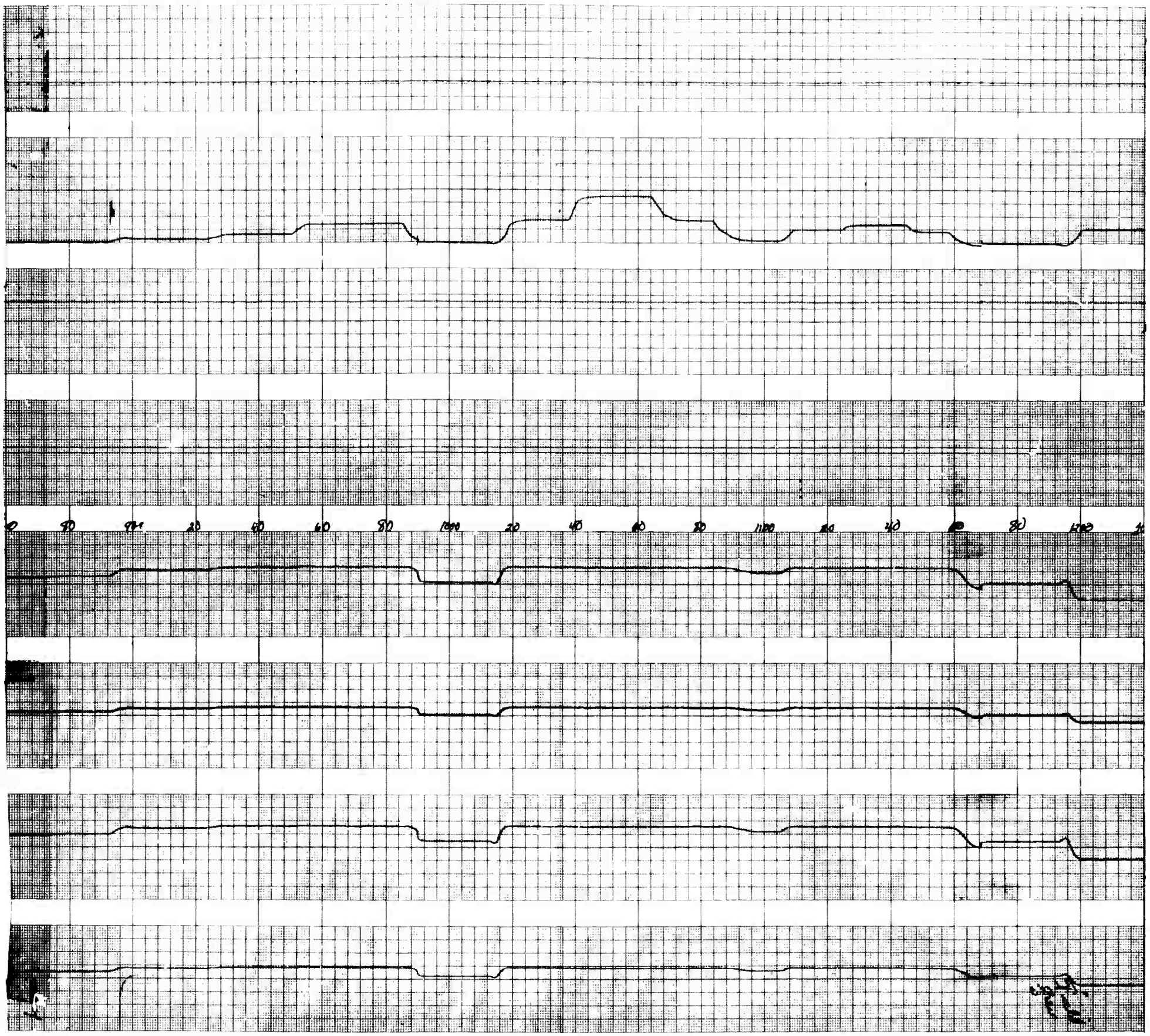

Figure 7. Original recording—run 8A.

Figure 7 shows a recording of a run (8A) with a very low seed fraction. The amplitude of the electrode output vibrations is nearly completely diminished. The helium mass flow also shows evidence that vibrations remain, even though the amplitude is very small. It is therefore impossible to correlate the two. If magnetic current (and, hence, magnetic field strength) is compared to the electrode output, it can be seen that after an increase in magnetic field beyond a certain value no further increase in output voltage is obtained. It is interesting to note that a slight overswing of the zero line of the magnet current generates an appreciable hump in the voltage output. (The wiring is made such that when reversing the magnet current, the current trace is not reversed—only the voltage output traces reverse.)

V. DISCUSSION OF RESULTS

VOLTAGE-CURRENT CURVES

Figure 8 shows a voltage-current curve for a generator with continuous electrodes. Figure 9 shows the related power output curve. These figures are a repetition of Figures 13 and 14 of the Fourth Quarterly Technical Summary Report (EDR 3861). The interpretation is now changed, however. In Figure 13 of EDR 3861, the points were connected by a curved line. Since direct plotted voltage-current curves were all straight lines, it no longer seems reasonable to connect the points in Figure 8 with a curved line.

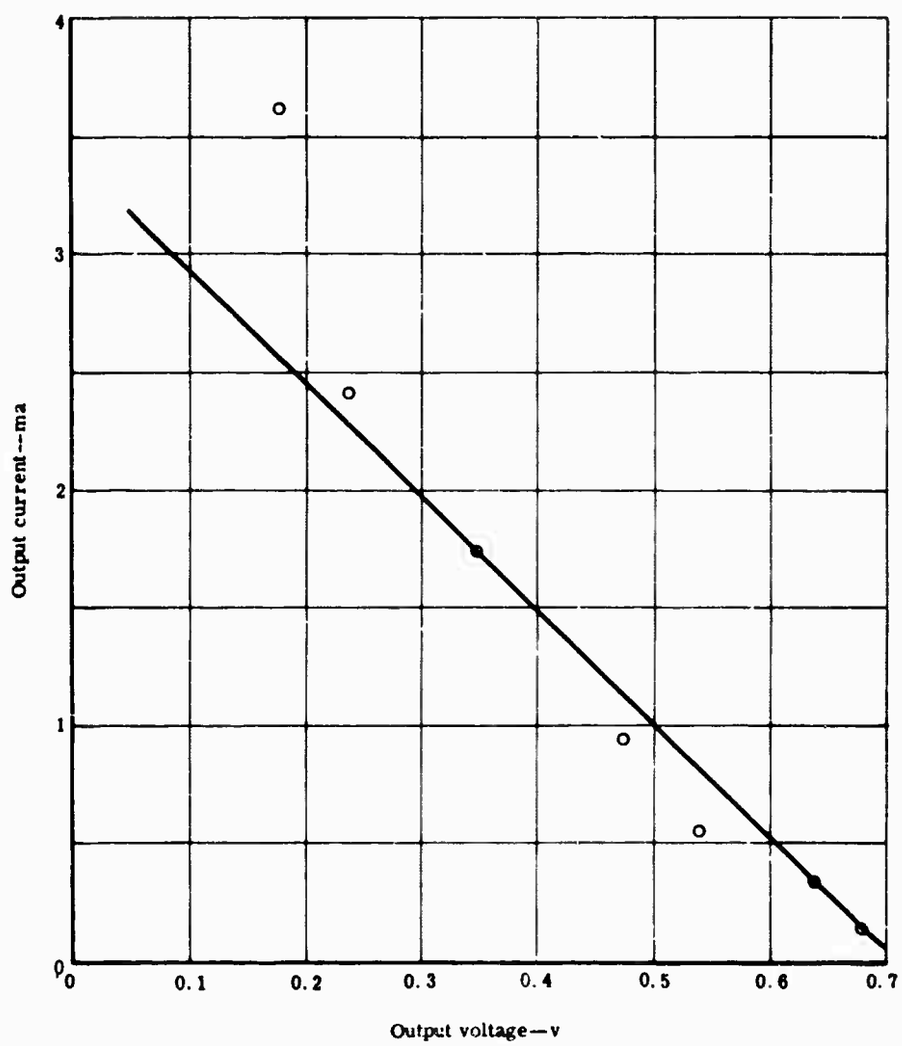

Figure 8. Voltage-current curve for generator with continuous electrodes.

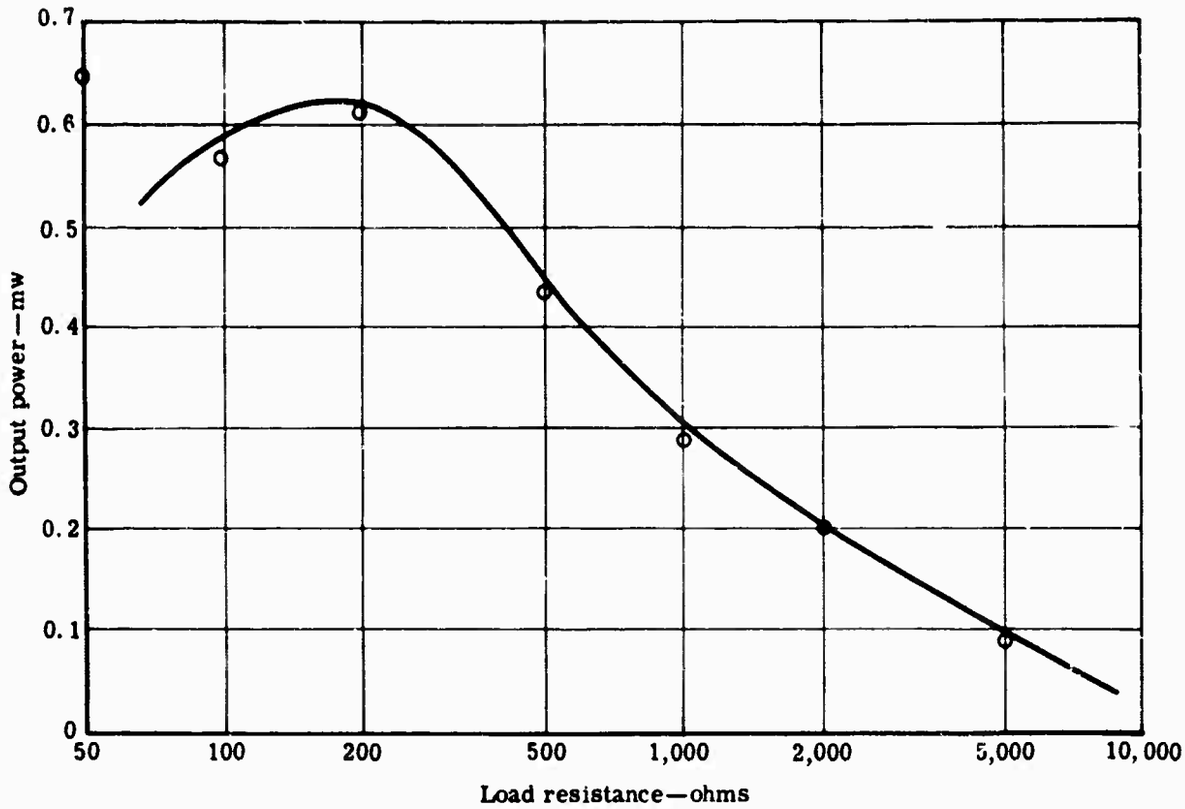

Figure 9. Power output curve for data of Figure 8.

Figure 10 shows a voltage-current curve for a segmented electrode generator; Figure 11 shows the related power output curve. Since the voltage-current curves are straight lines, the most important conclusion to be drawn is that the conductivity of the plasma does not depend on the current drawn. If electron heating had been observed, a definite dependence would have occurred between conductivity and current drawn.

For a first approximation, the internal resistance of the generator is found by dividing the open circuit voltage by the short circuit current. The internal resistance may also be found from the maximum of the power output curve. This gives an internal resistance for:

- The continuous electrode generator:
  - According to Figure 8:

$$R_I = \frac{0.72}{(3.4)(10^{-3})} = 210 \text{ ohms}$$

- According tc Figure 9:

$$R_I = 200 \text{ ohms}$$

- The segmented electrode generator:
  - According to Figure 10:

$$R_I = \frac{1.05}{(2.05)(10^{-2})} = 500 \text{ ohms}$$

  - According to Figure 11:

$$R_I = 500 \text{ ohms}$$

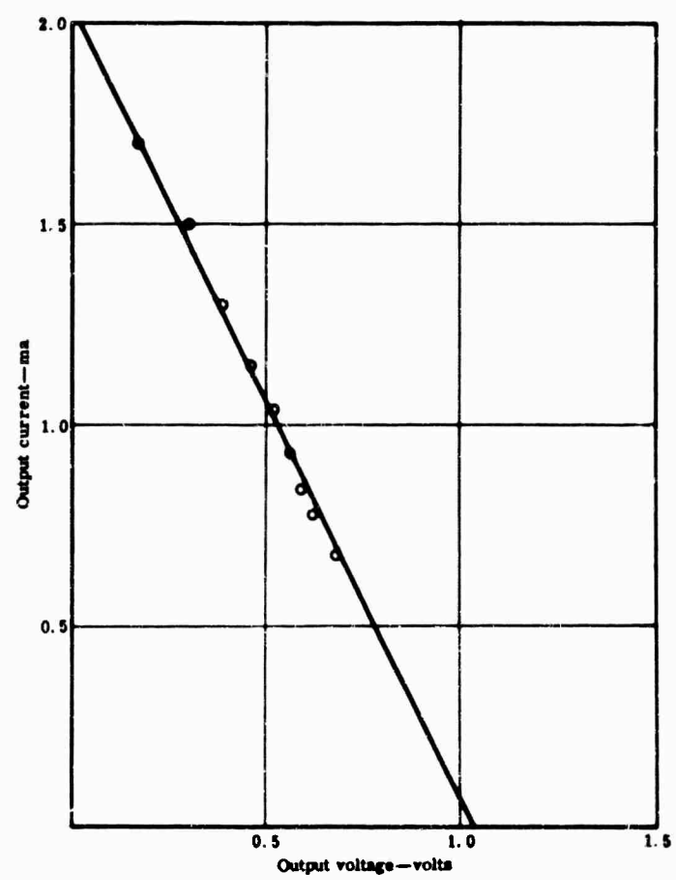

Figure 10. Voltage-current curve for generator with segmented electrodes.

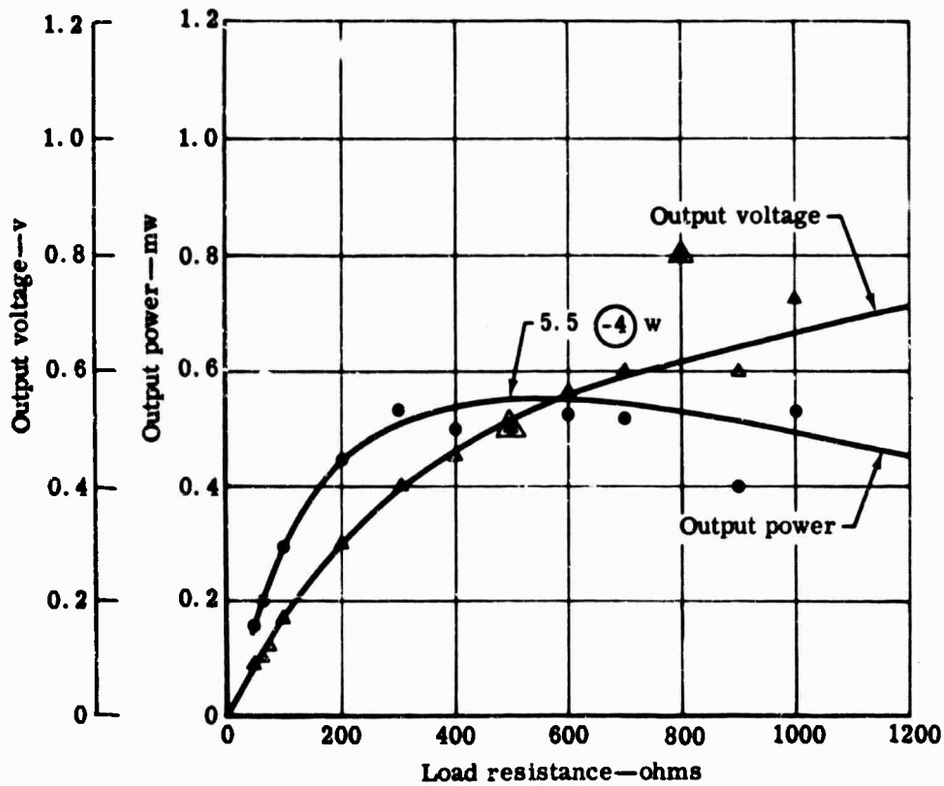

Figure 11. Power output curve for data of Figure 10.

These values may be too optimistic. Realistically, a leakage resistance does occur through the ceramic insulators or along the surface of these insulators. Also, the open circuit voltage is too low compared with the theoretical values. Therefore, an equivalent circuit, as shown in Figure 12, must be used.

For the case $R_L = 0$ (load resistor short circuited):

$$R_I = \frac{U_E}{I_L} \tag{1}$$

For the case $R_L = \infty$ (load resistor open),

$$R_S = \frac{U_L R_I}{U_E - U_L} \tag{2}$$

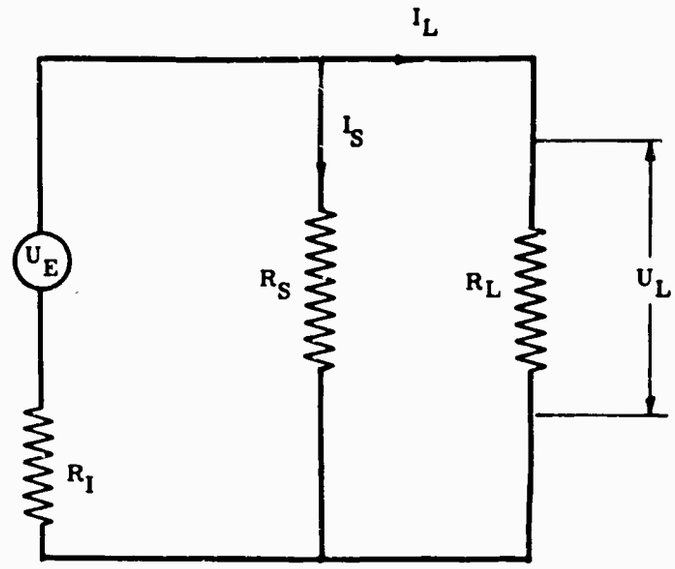

Figure 12. Faraday generator equivalent circuit.

Legend:

U_E —Electromotive force
R_I —Internal resistance
R_S —Shunt resistance due to leakage in and along insulator
R_L —Load resistor
U_L —Voltage across load resistor
I_L —Current through load resistor
I_S —Current through R_S

Assuming U_E = 14 v, for the case of the continuous electrodes generators, Equation (1) gives

$$R_I = \frac{14}{(3.4)(10^{-3})} = 4100 \text{ ohms}$$

and Equation (2) gives

$$R_S = \frac{(0.72)(4.1)(10^3)}{14 - 0.72} = 220 \text{ ohms}$$

for the case of the segmented electrode generator, Equation (1) gives

$$R_I = \frac{14}{(2.05)(10^{-3})} = 7000 \text{ ohms}$$

and Equation (2) gives

$$R_S = \frac{(1.05)(7)(10^3)}{14 - 1.05} = 560 \text{ ohms}$$

These numbers are, of course, alarming. The real internal resistance would be a factor of 12 to 18 higher as when assuming no leakage. This points out how important it is to know precisely the leakage resistance and the theoretical open circuit voltage. Efforts have been initiated to obtain this data more accurately. When deriving the equivalent circuit in Figure 12, the Hall effect was neglected. These numbers are thus taken from the most pessimistic viewpoint possible.

Therefore, for the case of the segmented electrodes, the equivalent circuit of Figure 13 seems to be more adequate. Since the Faraday generator (U_{EF1}) is shunted by R_{S1} and (U_{EF2}) is shunted by R_{S2}, this system can be regarded as a Hall generator (U_{EH}) with the internal resistance R_{IH} and with a load resistor R_{SH}. (R_{SH} is the leakage resistance between two adjacent electrodes.)

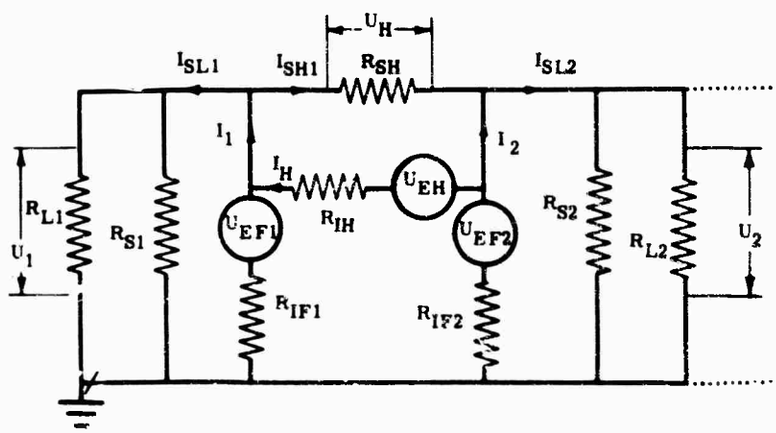

Legend:

U_{EF1} —Electromotive force of electrode 1 in faraday direction
U_{EF2} —Electromotive force of electrode 2 in faraday direction
U_{EH} —Electromotive force in Hall direction
R_{IF1} —Internal resistance in faraday direction for electrode 1
R_{IH} —Internal resistance in Hall direction for electrode 1
R_{L1} —Load resistance for electrode 1
R_{S1} —Shunt resistance for electrode 1
R_{SH} —Shunt resistance between two adjacent electrodes

Figure 13. Segmented electrode generator equivalent circuit.

In this report, Figure 13 is used only for qualitative information since the Hall voltage (U_H) and Hall current data necessary to calculate the R_{IH} and U_{EH} have not yet been obtained. Considering the fact that it should be approximately

$$U_{EH} = \omega \tau I_1 Bd \tag{3}$$

and considering the fact that the voltage-current curve—$U_1 = f(I_1)$—is a straight line, it can certainly be concluded that $R_{IH} \gg R_{IF1}$. R_{SH} may be small, however. In Figure 5, an observation is described which indicates that when shorting the load resistor on electrode 1, a decrease in output voltage can be observed on R_{L2} and all other load resistors simultaneously. This can be explained as follows. The current I_1 may take two different paths—through R_{S1} and R_{L1} and through R_{SH}, R_{S2}, and R_{L2}. Thus, from Figure 13, $I_1 = I_{SL1} + I_{SH1}$. If $R_{L1} = R_{L2}$ and $R_{S1} = R_{S2}$, then it follows that $I_{SL1} \gg I_{SH1}$, because it is understood that $R_{IF1} \ll R_{IH}$. Therefore only a small voltage drop across R_{SH}, which would make I_{SH1} flow, can be expected.

If R_{L1} is short circuited, which will automatically short circuit R_{S1} (leaving, however, R_{S2} and R_{L2} at the previous value), then I_2 is divided into two currents:

$$I_2 = I_{SL2} + I_{SH1}$$

Let the voltage observed before shorting R_L be U_2 and after shorting be U_2'. Then

$$U_2 = (I_2) \frac{R_{S2} R_{L2}}{R_{S2} + R_{L2}} \tag{4}$$

and

$$U_2' = (I_{SL2}) \frac{R_{S2} R_{L2}}{R_{S2} + R_{L2}} \tag{5}$$

Thus $U_2 > U_2'$, since $I_2 > I_{SL2}$, which was observed. To calculate the ratio $\frac{U_2}{U_2'}$, Equations (6) and (7) are used.

$$R_T = \frac{R_{S2} R_{L2}}{R_{S2} + R_{LS}} \tag{6}$$

and

$$R'_T = \frac{R_T R_{SH}}{R_T + R_{SH}} \tag{7}$$

Before shorting R_{S1}, the following relation holds:

$$U_2 = U_{EF2} \frac{R_T}{R_{IF2} + R_T} \tag{8}$$

assuming that $R_{IF2} = R_{IF1}$, $U_{EF1} = U_{EF2}$, and $R_{IH} \gg R_{IF1}$.

After shorting R_{S1}, the following relation is obtained

$$U'_2 = U_{EF2} \frac{R'_T}{R_{IF2} + R'_T} \tag{9}$$

For the ratio of the two relations,

$$\frac{U_2}{U'_2} = \frac{R_T (R_{IF2} + R'_T)}{(R_{IF2} + R_T) R'_T} \tag{10}$$

For an approximate calculation, it is assumed that $R_{IF2} \gg R'_T$ and R_T.

$$R_{SH} = R_T \left(\frac{U'_2}{U_2 - U'_2} \right) \tag{11}$$

In Figure 5, the following values were observed:

U_2 = 1.60 volts

U'_2 = 1.50 volts

R_{L2} = 500 ohms

R_{S2} = 500 ohms

therefore

$$R_{SH} = 250 \left(\frac{1.50}{1.60 - 1.50}\right) = 3750 \text{ ohms}$$

Without the approximation of Equation (11), the value of the leakage resistance between two electrodes is

$$R_{SH} = R_T \frac{U_2' R_I}{U_2 (R_I + R_T) - U_2' (R_I + R_T)} \tag{12}$$

With $R_I = 7000$ ohms,

$$R_{SH} = (250) \frac{(1.50)(7)(10^3)}{1.6(7.25)(10^3) - 1.5(7.25)(10^3)} = 3650 \text{ ohms}$$

These, of course, are only approximate values. More runs are necessary to determine R_{SH} more precisely.

SATURATION EFFECT

Figure 14 shows the output voltage across a 100-ohm load resistor for continuous electrodes. Figure 15 shows the same for segmented electrodes. Both curves are similar, following a straight line, then deviating, and finally saturating. According to Figure 12 the output voltage across a load resistor should be

$$U_L = \frac{R_L}{R_I + R_L} v Bd \tag{13}$$

Neglecting the Hall effect, the voltage U_L should be proportional to B. As Figures 14 and 15 show, this is only true for small values of B. For higher values apparently the internal resistance R_I becomes a function of B.

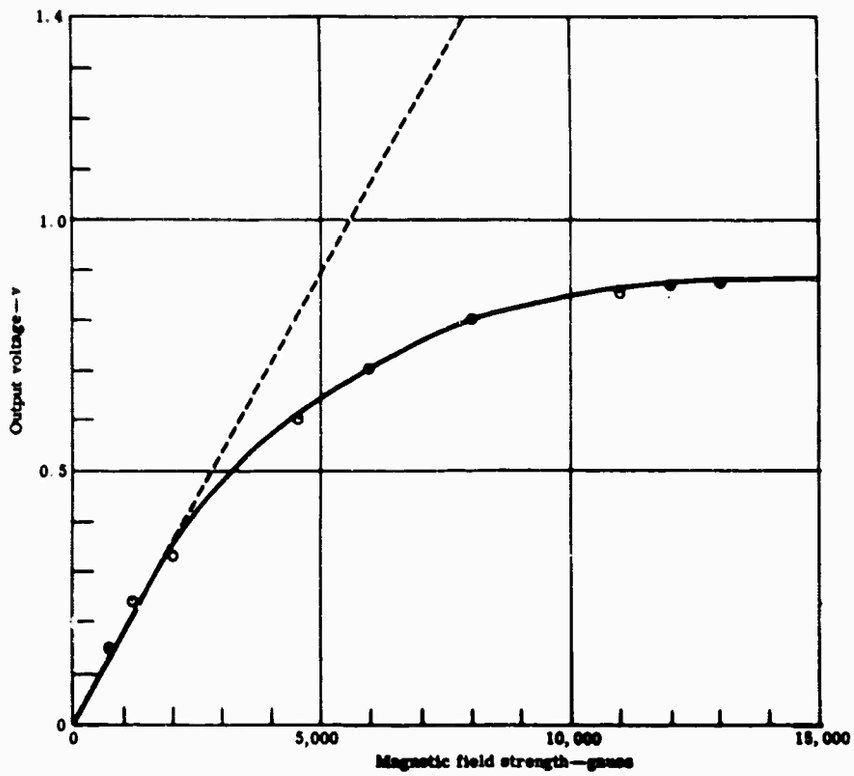

Figure 14. Saturation effect for continuous electrode generator.

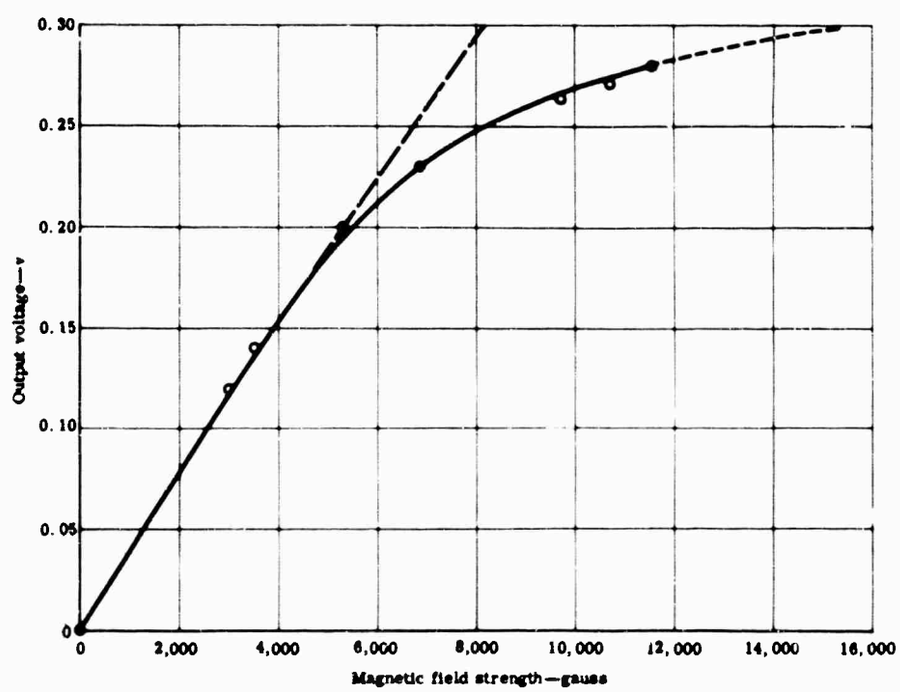

Figure 15. Saturation effect for segmented electrode generator.

The elementary theory based on Ohm's Law with Hall-effect yields, for the interior resistance for one electrode pair,

$$R_I = \frac{d}{bl} \sigma^{-1} \; f(d, l, \omega\tau) \sqrt{1 + \omega^2 \tau^2} \tag{14}$$

where

b = electrode width
l = electrode length
d = electrode distance
σ = conductivity
ω = electron cyclotron frequency
τ = electron collision frequency

The factor f takes account of the duct geometry. For $\omega\tau = 1$, $f \equiv f_o = 1$; for $\omega\tau \gg 1$ $f \equiv f_\infty =$ a constant.

Since, however,

$$\omega = \frac{e\,B}{m_e}$$

for large values of B— $\omega\tau \gg 1$ and $R_I \gg R_L$ from Equations (13) and (14)—

$$U_L = U_{saturation} = \left(\frac{m_e}{e}\right)\left(\frac{bl}{f}\right)\left(\frac{\sigma}{\tau}\right)(v)\,(R_L) \tag{15}$$

In this case, U_L is no longer dependent upon B, since for $\omega\tau \gg 1$, f = a constant, which explains the observed saturation for high values of B.

From Equation (14), and from the conditions $\omega\tau \gg 1$ and $R_I \gg R_L$ for the critical magnetic field at which saturation is to be observed,

$$B = B_{saturation} \gg \frac{m_e}{e} \; (f_\infty \tau)^{-1} \; \frac{R_L}{R_{IO}} \tag{16}$$

where

$$R_{IO} = \frac{d}{bl} \sigma^{-1} = \text{the interior resistance in absence of Hall effect}$$

For low values of B, the slope of the straight lines can be calculated according to Figure 12.

$$\frac{U_L}{B} = v\,d. \quad \frac{\dfrac{R_S R_L}{R_S + R_L}}{R_I + \dfrac{R_S R_L}{R_S + R_L}} \tag{17}$$

This allows either the gas velocity or the internal resistance to be determined:

$$v = \frac{1}{d} \frac{U_L}{B} \frac{R_I + \dfrac{R_S R_L}{R_S + R_L}}{\dfrac{R_S R_L}{R_S + R_L}} \tag{18}$$

and

$$R_I = \left(\frac{B}{U_L} \quad vd - 1 \right) \frac{R_S R_L}{R_S + R_L} \tag{19}$$

In the case of Figure 14, the following numbers are valid:

$$\frac{B}{U_L} = 0.55 \left[\frac{T}{v} \right]$$

$$R_S = 200 \text{ ohms}$$

$$R_L = 100 \text{ ohms}$$

$$d = 1.5 \times 10^{-2} \text{ m}$$

$$v = 1.3 \times 10^{3} \text{ m/sec}$$

where

$$T = 1.0 \text{ weber/m}^2$$

Therefore

$$R_I = (0.66)(10^2)(0.55)(1.3 \times 10^3)(1.5)(10^{-2}) - (0.66)(10^2) = 650 \text{ ohms}$$

Upon comparing this value of 650 ohms with the 4000 ohms derived from Figure 8, it is found that the internal resistance is indeed increased when B is increased. Figure 8 is taken at 8000 gauss, where the deviation from the straight line already is appreciable.

To measure the velocity, several voltage-current curves must be run at low values of B, so long as the real curve does not deviate from the straight line. After considering the leakage resistance, R_I can be determined rather precisely. Then, using Equation (18), the gas velocity can be determined.

CONCLUSIONS

The primary results of this investigation are:

- A saturation effect of the power output was observed. Above the magnetic field strength of 10,000 gauss, the power output increases only slightly and finally saturates. This effect has been observed for both continuous and segmented electrodes. The investigation and elimination of this effect by additional experiments is the most important objective in the coming program.
- All observed voltage-current curves are straight lines. This is true for directly plotted curves as well as for curves compiled from different runs. The straight lines indicate that no appreciable electron heating (magnetically induced ionization) has been observed.
- Neglecting possible leak resistance and boundary layer effects, the observed conductivity is 1 mho/m for a gas temperature of 1700°K. This is very close to the equilibrium conductivity.
- Although most of the observed data are explained analytically, additional test data are needed to confirm that observations to date are interpreted correctly.

BLANK PAGE

DISTRIBUTION LIST

	No. Copies
Office of Naval Research Power Branch (Code 429) Washington, D. C. 20360 Attn: John A. Satkowski	6
Commanding Officer Office of Naval Research Branch Office Box 39 Navy #100 Fleet Post Office New York, New York	1
Office of Naval Research Branch Office The John Crerar Library Building 86 East Randolph Street Chicago 1, Illinois	1
Chief, Bureau of Ships Washington, D. C. 20360 Attn: Dr. John Huth, Chief Scientist	1
U.S. Naval Research Laboratory Washington, D. C. 20390 Attn: Technical Information Division	6
Director Advanced Research Projects Agency Material Sciences Division Washington, D. C. 20301	1
Wright-Patterson Air Force Base Aeronautical Systems Division Ohio Attn: Don Warnock (ASRMFP-2)	1

	No. Copies
Air Force Office of Scientific Research Washington 25, D. C. Attn: Dr. Milton M. Slawsky	1
U. S. Naval Ordnance Test Station Propulsion Applied Research Group China Lake, California Attn: Mr. Leroy J. Krzycki (Code 4506)	1
Rome Air Development Center Rome, New York Attn: Mr. Frank J. Mellura	1
U. S. Naval Ordnance Laboratory NA Division White Oak, Maryland	
Attn: Wallace Knutsen	1
Library	2
Defense Documentation Center Cameron Street Alexandria, Virginia 22314	20
U. S. Army Research & Development Laboratory Fort Belvoir, Virginia Attn: Frank Shields (ERD-EP)	1
National Aeronautics and Space Administration Lewis Research Center 21000 Brookpark Road Cleveland 35, Ohio	
Attn: John Stevens	1
Dr. B. Lubarsky	1

	No. Copies
U.S. Atomic Energy Commission Division of Reactor Development Direct Energy Conversion Section, RD; AED Germantown, Maryland	1
Dr. T. Brogan AVCO-Everett Research Laboratory 2385 Revere Beach Parkway Everett, Massachusetts	1
Dr. B. Zauderer General Electric Company Valley Forge Space Technical Center Philadelphia 1, Pennsylvania	1
Dr. M. E. Talaat Department of Mechanical Engineering University of Maryland College Park, Maryland	1
Dr. W. D. Jackson Electrical Engineering Department Massachusetts Institute of Technology Cambridge 39, Massachusetts	1
Dr. B. C. Lindley Nuclear Research Centre C. A. Parsons & Company, Ltd. Fossway, Newcastle Upon Tyne 6 England	1
Dr. Robert Eustis Thermosciences Division Stanford University Stanford, California	1

	No. Copies
Mr. John Wright Central Electricity Research Laboratories Cleeve Road, Leatherhead, Surrey England	1
Dr. Richard Schamberg Rand Corporation 1700 S. Main Street Santa Monica, California	1
Dr. W. S. Emmerich Westinghouse Research Laboratories Beulah Road, Churchill Borough Pittsburgh 35, Pennsylvania	1
Dr. R. T. Schneider Allison Division General Motors Corporation Indianapolis, Indiana	1
Dr. D. G. Elliott Jet Propulsion Laboratory Pasadena, California	1
Dr. John J. Connelly, Jr. State University of New York College at Fredonia Physics Department Fredonia, New York 14063	1